# Topology-Driven Magnetic Quantum Phase Transition in Topological Insulators

Jinsong Zhang *et al.*

*Science* **339**, 1582 (2013);
DOI: 10.1126/science.1230905

haplotypes and for categories related to glycosylation among genes with a shared coding SNP (tables S9 and S14).

Given that viruses frequently use host glycans to gain entry into host cells and some bacteria imitate host glycans to evade the host immune system (*33*–*35*), these enrichments suggest that the targets of balancing selection that we identified likely evolved in response to pressures exerted by human and chimpanzee pathogens, mirroring what is known about other genes under balancing selection in humans [(*1*, *17*, *18*, *36*) and references therein]. Moreover, the observation that variation at loci that lie at the interface of host-pathogen interactions was stably maintained for millions of years is consistent with the hypothesis that arms races between hosts and pathogens can result not only in transient polymorphisms but also, in the presence of a cost to resistance, to a stable limit cycle in allele frequencies in the host (*4*, *9*, *37*).

We found several instances of ancient balancing selection in humans in addition to the two previously known cases. Our analysis suggests that this mode of selection has not only involved protein changes but also the regulation of genes involved in the interactions of humans and chimpanzees with pathogens and points to membrane glycoproteins as frequent targets. Because we deliberately focused on the subset of cases of balancing selection that are the least equivocal—requiring variation at two or more sites to be stably maintained in the two species from their split to the present—we likely missed balanced polymorphisms with a high mutation rate to new selected alleles [that is, with high allelic turnover (*38*)], in which the ancestral segment has been too heavily eroded by recombination, as well as any instance in which balancing selection pressures are more recent than the human-chimpanzee split. Thus, it seems likely that many more cases of balancing selection in the human genome remain to be found.

### References and Notes


1. P. W. Hedrick, *Heredity (Edinb.)* **107**, 283 (2011).
2. D. G. Reid, *Biol. J. Linn. Soc. Lond.* **30**, 1 (1987).
3. L. D. Gigord, M. R. Macnair, A. Smithson, *Proc. Natl. Acad. Sci. U.S.A.* **98**, 6253 (2001).
4. E. A. Stahl, G. Dwyer, R. Mauricio, M. Kreitman, J. Bergelson, *Nature* **400**, 667 (1999).
5. S. Wright, *Genetics* **24**, 538 (1939).
6. T. Hiwatashi *et al.*, *Mol. Biol. Evol.* **27**, 453 (2010).
7. Heliconious Genome Consortium, *Nature* **487**, 94 (2012).
8. R. Ghosh, E. C. Andersen, J. A. Shapiro, J. P. Gerke, L. Kruglyak, *Science* **335**, 574 (2012).
9. B. Charlesworth, D. Charlesworth, *Elements of Evolutionary Genetics* (Roberts and Company, Greenwood Village, CO, 2010).
10. T. Dobzhansky, *Genetics of the Evolutionary Process* (Columbia Univ. Press, New York, 1970).
11. R. C. Lewontin, *The Genetic Basis of Evolutionary Change* (Columbia Univ. Press, New York, 1974).
12. J. H. Gillespie, *The Causes of Molecular Evolution* (Oxford Univ. Press, Oxford, 1991).
13. R. R. Hudson, N. L. Kaplan, *Genetics* **120**, 831 (1988).
14. D. Charlesworth, *PLoS Genet.* **2**, e64 (2006).
15. C. Wiuf, K. Zhao, H. Innan, M. Nordborg, *Genetics* **168**, 2363 (2004).
16. Materials and methods are available as supplementary materials on *Science* Online.
17. J. Klein, Y. Satta, C. O'HUigin, N. Takahata, *Annu. Rev. Immunol.* **11**, 269 (1993).
18. L. Ségurel *et al.*, *Proc. Natl. Acad. Sci. U.S.A.* **109**, 18493 (2012).
19. K. L. Bubb *et al.*, *Genetics* **173**, 2165 (2006).
20. The 1000 Genomes Project Consortium, *Nature* **467**, 1061 (2010).
21. A. Auton *et al.*, *Science* **336**, 193 (2012).
22. N. Patterson, D. J. Richter, S. Gnerre, E. S. Lander, D. Reich, *Nature* **441**, 1103 (2006).
23. A. Hodgkinson, A. Eyre-Walker, *Nat. Rev. Genet.* **12**, 756 (2011).
24. M. Franchini, F. Capra, G. Targher, M. Montagnana, G. Lippi, *Thromb. J.* **5**, 14 (2007).
25. C. Gieger *et al.*, *Nature* **480**, 201 (2011).
26. W. Y. Ko *et al.*, *Am. J. Hum. Genet.* **88**, 741 (2011).
27. S. Kudo, M. Fukuda, *J. Biol. Chem.* **265**, 1102 (1990).
28. D. Nagakubo *et al.*, *J. Immunol.* **171**, 553 (2003).
29. J. Monnier, M. Samson, *FEBS J.* **275**, 4014 (2008).
30. P. A. Videira *et al.*, *Glycoconj. J.* **25**, 259 (2008).
31. J. J. Priatel *et al.*, *Immunity* **12**, 273 (2000).
32. J. M. Johnsen *et al.*, *Mol. Biol. Evol.* **26**, 567 (2009).
33. P. Gagneux, A. Varki, *Glycobiology* **9**, 747 (1999).
34. S. Olofsson, T. Bergström, *Ann. Med.* **37**, 154 (2005).
35. C. J. Day, E. A. Semchenko, V. Korolik, *Front. Cell. Infect. Microbiol.* **2**, 9 (2012).
36. C. Ruwende *et al.*, *Nature* **376**, 246 (1995).
37. A. Tellier, J. K. Brown, *Proc. Biol. Sci.* **274**, 809 (2007).
38. N. Takahata, *Proc. Natl. Acad. Sci. U.S.A.* **87**, 2419 (1990).
39. Chimpanzee Sequencing and Analysis Consortium, *Nature* **437**, 69 (2005).
40. T. Zeller *et al.*, *PLoS ONE* **5**, e10693 (2010).



**Acknowledgments:** We thank D. Conrad, Y. Lee, M. Nobrega, J. Pickrell, and H. Shim as well as A. Kermany, A. Venkat, and other members of the PPS labs for helpful discussions; I. Aneas, M. Çalışkan, M. Nobrega, and C. Ober for their assistance with experiments; and G. Coop for discussions and comments on an earlier version of this manuscript. E.M.L. was supported in part by NIH training grant T32 GM007197. This work was supported by NIH HG005226 to J.D.W.; Israel Science Foundation grant 1492/10 to G.S.; a Wolfson Royal Society Merit Award, a Wellcome Trust Senior Investigator award (095552/Z/11/Z), and Wellcome Trust grants 090532/Z/09/Z and 075491/Z/04/B to P.D.; Wellcome Trust grant 086084/Z/08/Z to G.M.; and NIH grant GM72861 to M.P. M.P. is a Howard Hughes Medical Institute Early Career Scientist. The data set of shared SNPs is available from http://przeworski.uchicago.edu/wordpress/?page_id=20. Data from the validation experiment are available from GenBank under accession nos. KC541701 to KC542146. The biological material obtained from the San Diego Zoo and used in this study is subject to a materials tranfer agreement.


### Supplementary Materials

www.sciencemag.org/cgi/content/full/science.1234070/DC1
Materials and Methods
Figs. S1 to S9
Tables S1 to S20
References


13 December 2012; accepted 1 February 2013
Published online 14 February 2013;
10.1126/science.1234070




# REPORTS

# Topology-Driven Magnetic Quantum Phase Transition in Topological Insulators


Jinsong Zhang,[1]* Cui-Zu Chang,[1,2]* Peizhe Tang,[1]* Zuocheng Zhang,[1] Xiao Feng,[2] Kang Li,[2] Li-li Wang,[2] Xi Chen,[1] Chaoxing Liu,[3] Wenhui Duan,[1] Ke He,[2]† Qi-Kun Xue,[1,2] Xucun Ma,[2] Yayu Wang[1]†



The breaking of time reversal symmetry in topological insulators may create previously unknown quantum effects. We observed a magnetic quantum phase transition in Cr-doped $Bi_2(Se_xTe_{1-x})_3$ topological insulator films grown by means of molecular beam epitaxy. Across the critical point, a topological quantum phase transition is revealed through both angle-resolved photoemission measurements and density functional theory calculations. We present strong evidence that the bulk band topology is the fundamental driving force for the magnetic quantum phase transition. The tunable topological and magnetic properties in this system are well suited for realizing the exotic topological quantum phenomena in magnetic topological insulators.


The metallic surface states of three-dimensional (3D) topological insulators (TIs) are protected by time reversal symmetry (TRS) (*1*–*3*). Although breaking the TRS is generally detrimental to these states, it may also lead to exotic topological quantum effects. Examples include image magnetic monopoles (*4*), a quantized anomalous Hall effect (*5*, *6*), giant magneto-optical effects (*7*), and a dissipationless inverse spin-Galvanic effect (*8*). A key step for realizing these previously unknown quantum states is to tune the magnetic ordering in TIs in a controlled manner and investigate the interplay between magnetism and topological order.

With their large bulk gap and a single-surface Dirac cone, $Bi_2Te_3$ and $Bi_2Se_3$ (*9*–*11*) are widely used as hosts for TRS-breaking perturbations. In Mn-doped $Bi_2Te_3$ single crystals, magnetization


[1]State Key Laboratory of Low Dimensional Quantum Physics, Department of Physics, Tsinghua University, Beijing 100084, P. R. China. [2]Institute of Physics, Chinese Academy of Sciences, Beijing 100190, P. R. China. [3]Department of Physics, the Pennsylvania State University, University Park, PA 16802–6300, USA.

*These authors contributed equally to this work.
†Corresponding author. E-mail: kehe@aphy.iphy.ac.cn (K.H.); yayuwang@tsinghua.edu.cn (Y.W.)

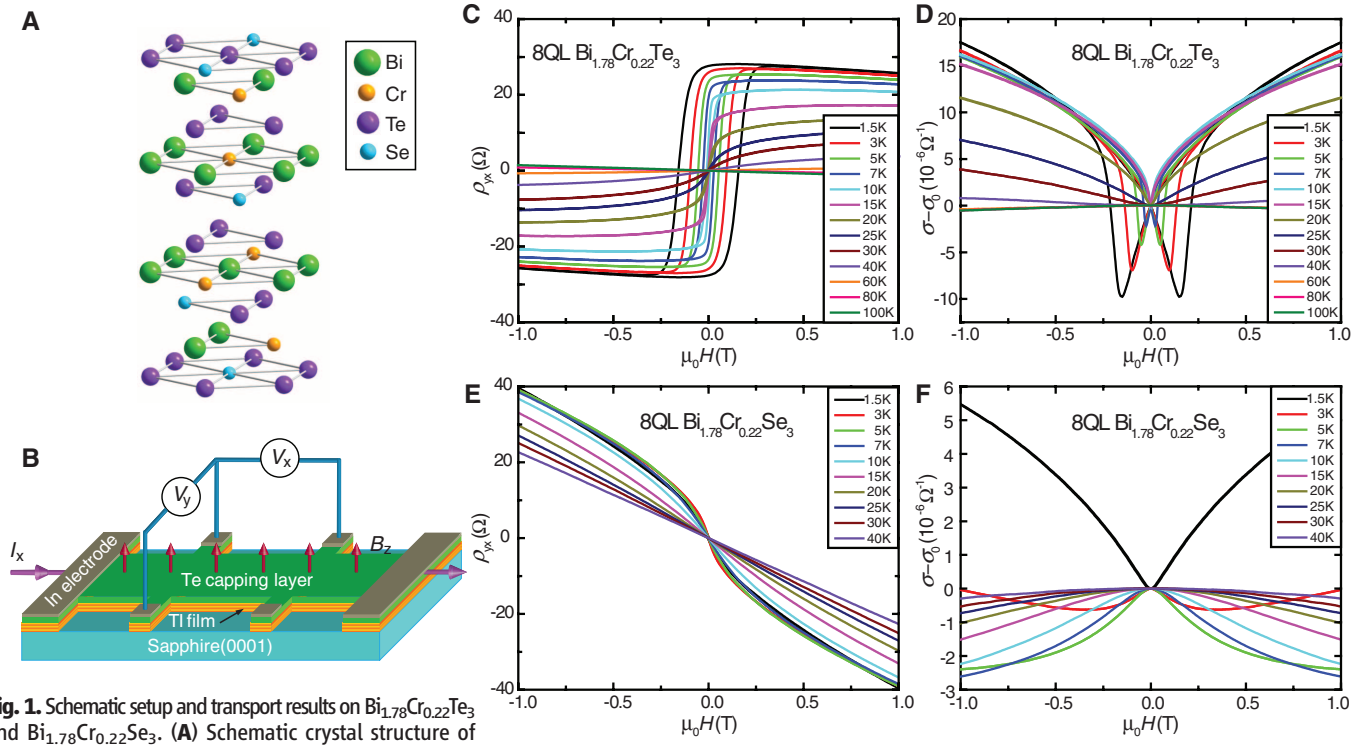


**Fig. 1.** Schematic setup and transport results on $Bi_{1.78}Cr_{0.22}Te_3$ and $Bi_{1.78}Cr_{0.22}Se_3$. (**A**) Schematic crystal structure of $Bi_{2-y}Cr_y(Se_xTe_{1-x})_3$ (two QLs are shown). (**B**) Schematic device for the magneto transport measurements. (**C**) The Hall effect of $Bi_{1.78}Cr_{0.22}Te_3$ film shows hysteretic loops below $TC$ = 20 K with a positive AHE term, and (**D**) the MC curves show a butterfly-shaped hysteresis pattern. (**E**) In the $Bi_{1.78}Cr_{0.22}Se_3$ film, the Hall effect shows a negative curvature without hysteresis. (**F**) The MC curves display a WL-to-WAL crossover.

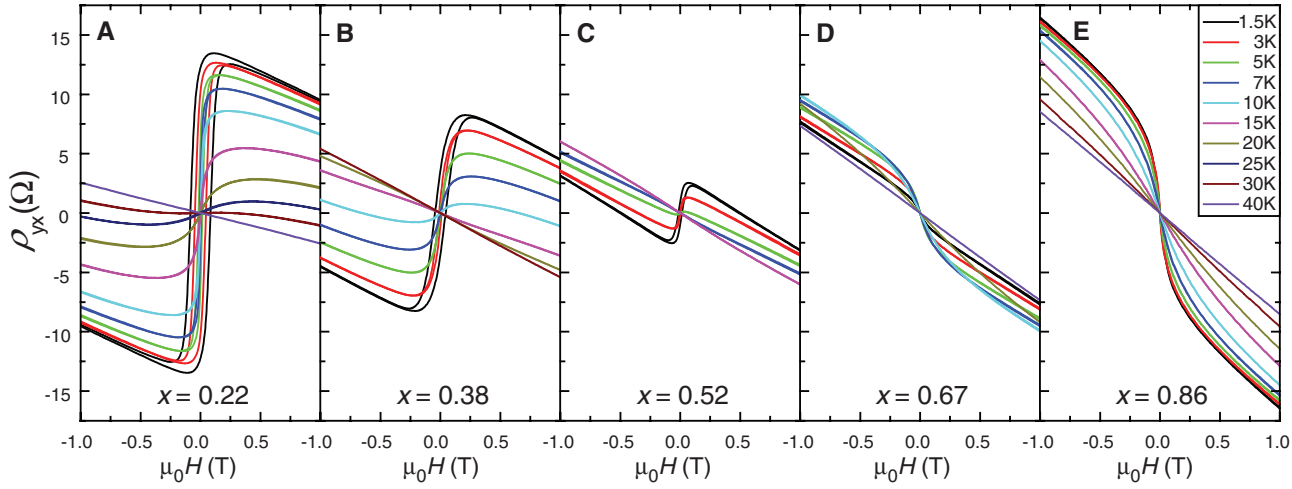


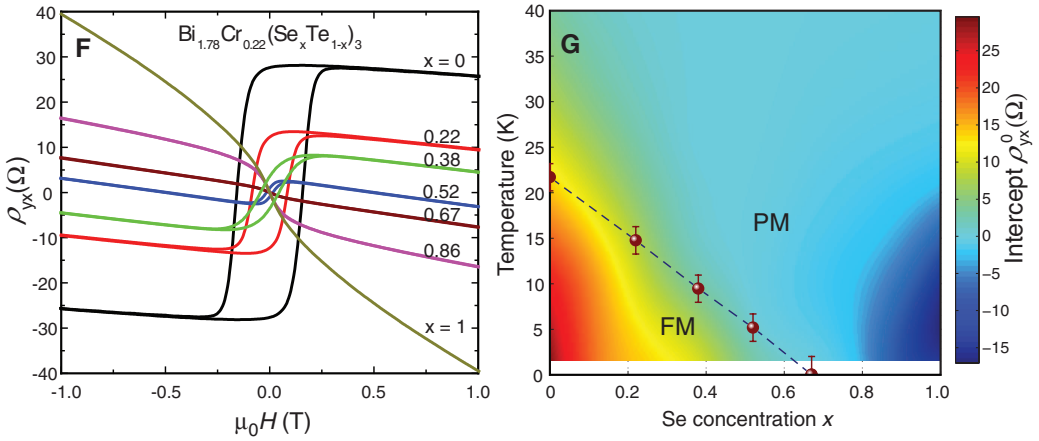


**Fig. 2.** The magnetic QPT in the $Bi_{1.78}Cr_{0.22}(Se_xTe_{1-x})_3$ films. (**A** to **E**) Field-dependent Hall traces of $Bi_{1.78}Cr_{0.22}(Se_xTe_{1-x})_3$ films with $0.22 \le x \le 0.86$ measured at varied temperatures. (**F**) Systematic evolution of the Hall effect of all the samples ($0 \le x \le 1$) measured at $T$ = 1.5 K. (**G**) Magnetic phase diagram of $Bi_{1.78}Cr_{0.22}(Se_xTe_{1-x})_3$ summarizing the intercept $\rho_{yx}^0$ as a function of $x$ and $T$. The $TC$ of the FM phase is indicated by the solid symbols.

measurements demonstrate a ferromagnetic (FM) state with a Curie temperature ($T_C$) of up to 12 K (*12*). On the cleaved surface of an Fe-doped $Bi_2Se_3$ single crystal, angle-resolved photoemission spectroscopy (ARPES) reveals the opening of an energy gap at the Dirac point (*13*). Iron (Fe) atoms deposited on the surface of a $Bi_2Se_3$ single crystal are found to create odd multiples of Dirac-like surface states (*14*). Scanning tunneling microscopy on the surface of magnetically doped TI crystals demonstrates that breaking TRS can lead to previously unknown quasiparticle interference patterns (*15*) and strong spatial variations for the helical surface states (*16*).

Most of these previous studies focused on the effect of magnetism on the topological surface states; however, little is known about how the magnetic ordering is affected by the topological property. Because the $Z_2$ bulk topology is the most fundamental identity of a TI, it probably also plays a role in determining the phases and phase transitions in magnetically doped TIs. To test this conjecture, we fabricated chromium (Cr)–doped $Bi_2(Se_xTe_{1-x})_3$ TI films using molecular beam epitaxy (*17*). By varying the mixing ratio of $Bi_2Se_3$ and $Bi_2Te_3$, we can actively modify the strength of spin-orbit coupling (SOC), which is essential for the band inversion of TIs. In the resulting $Bi_{2-y}Cr_y(Se_xTe_{1-x})_3$ (Fig. 1A), the Cr dopants substitute Bi sites, and Se/Te atoms are randomly mixed. All of the films have the same thickness $d$ = 8 quintuple layers (QLs), so that they are in the 3D regime with decoupled surfaces (*18*). The Cr content is fixed at $y$ = 0.22 because at this doping level, the density of local moments is high enough to sustain long-range magnetic order, and the SOC strength is reduced to the verge of a topological phase transition (*19*).

Magneto transport measurements on the TI films (Fig. 1B) are made in the presence of an external magnetic field ($H$) perpendicular to the film plane. At the base temperature $T$ = 1.5 K, the Hall effect of the 8-QL $Bi_{1.78}Cr_{0.22}Te_3$ film (Fig. 1C) shows a hysteretic loop and a nearly square-shaped positive jump, the hallmarks of anomalous Hall effect (AHE) in FM conductors (*20*). The total 2D Hall resistivity $\rho_{yx}$ can be expressed as $\rho_{yx} = R_A M(T, H) + R_N H$, where $M(T, H)$ is the magnetization and $R_A$ and $R_N$ are the anomalous and normal Hall coefficients, respectively. Both the anomalous Hall resistivity and the coercive force ($H_{coer}$) decrease as $T$ rises. The Hall traces become fully reversible at $T >$ 20 K; thus, the $T_C$ of this film is around 20 K. The normal Hall effect at high $H$ has a negative slope for the entire temperature range (fig. S2), indicating the existence of electron-type charge carriers. The magnetoconductivity (MC) curves taken at $T < T_C$ show butterfly-shaped hysteresis at weak $H$ (Fig. 1D), as commonly observed in FM metals. MC keeps increasing at higher $H$, which is indicative of the weak localization (WL) of charge carriers instead of the weak antilocalization (WAL) in pristine $Bi_2Te_3$ (*21*).

The Cr-doped $Bi_2Se_3$ exhibits a very different transport behavior. At $T$ = 1.5 K, the Hall trace of $Bi_{1.78}Cr_{0.22}Se_3$ film (Fig. 1E) has a pronounced negative curvature at weak $H$ but shows no observable hysteresis, which is consistent with the field-induced AHE in paramagnetic (PM) materials without spontaneous magnetization. The MC curves also show no sign of hysteresis even at the base temperature (Fig. 1F). MC changes from positive at low $T$ to negative at high $T$, which is consistent with the WL-to-WAL crossover reported previously (*22*). The possible existence of in-plane ferromagnetism in the $Bi_{1.78}Cr_{0.22}Se_3$ film is ruled out by magnetization and magneto transport

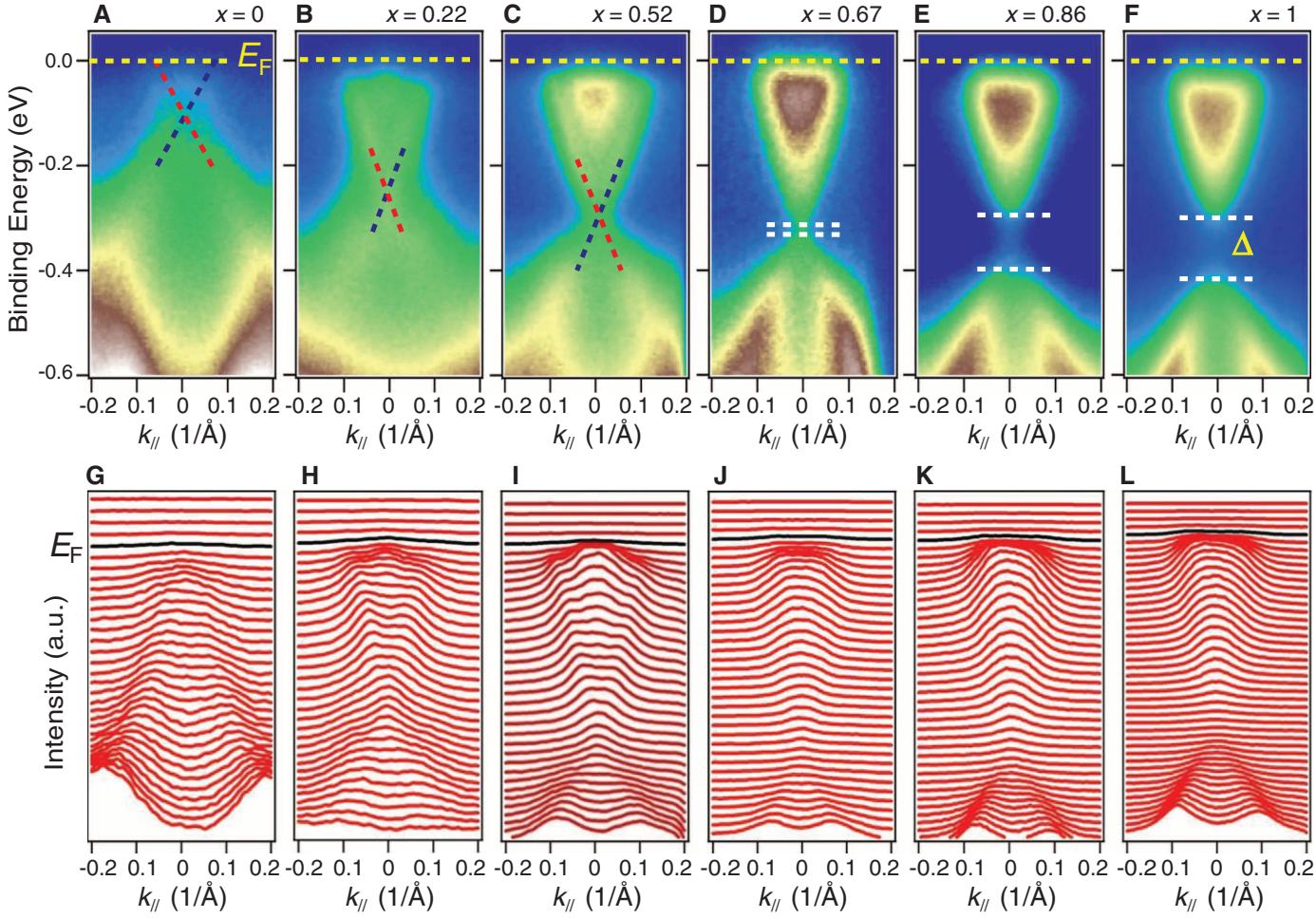


**Fig. 3.** ARPES measurements on $Bi_{1.78}Cr_{0.22}(Se_xTe_{1-x})_3$ films. (**A** to **F**) ARPES band maps and (**G** to **L**) the MDCs taken at 120 K along the K-Γ-K direction on $Bi_{1.78}Cr_{0.22}(Se_xTe_{1-x})_3$, with $x$ = 0, 0.22, 0.52, 0.67, 0.86 and 1.0. The blue and red dashed lines in (A) to (C) indicate the surface states with opposite spin polarities. In (D) to (F), an energy gap Δ opens between the bulk valence band and conduction band.

measurements with $H$ applied along the film plane (fig. S12).

To uncover the origin of the sharp contrast between the magneto transport properties of Cr-doped $Bi_2Te_2$ and $Bi_2Se_3$, we fabricated Cr-doped $Bi_2(Se_xTe_{1-x})_3$, an isostructural, isovalent mixture of $Bi_2Te_3$ and $Bi_2Se_3$. The Hall traces are displayed in Fig. 2, A to E, measured on five $Bi_{1.78}Cr_{0.22}(Se_xTe_{1-x})_3$ films with $0.22 \leq x \leq 0.86$. The three Te-rich samples with $x \leq 0.52$ all show a hysteretic response at low $T$, reflecting FM ordering. As the Se content is increased to $x = 0.67$, however, the hysteresis disappears, and the system becomes PM. The sign of the AHE also reverses to negative right at this doping. With further increase of $x$ to 0.86, the system remains PM, and the negative AHE becomes more pronounced. The FM-to-PM phase transition can also be seen in the MC curves (fig. S4) (*17*).

The Hall curves of all the $Bi_{1.78}Cr_{0.22}(Se_xTe_{1-x})_3$ films measured at $T = 1.5$ K are summarized in Fig. 2F, revealing a highly systematic evolution of $H_{coer}$ and the intercept Hall resistivity $\rho_{yx}^0$ (fig. S6A). Because the magnetism of the system can be characterized by the AHE, we can construct a magnetic phase diagram by plotting the $\rho_{yx}^0$ values of each sample and at each $T$ (Fig. 2G). At the base temperature, the phase diagram is separated into two distinct regimes: an FM phase with positive $\rho_{yx}^0$ and a PM phase with negative $\rho_{yx}^0$. Because the transition between the two magnetic phases occurs at the ground state, it is a quantum phase transition (QPT) driven by the change of chemical composition. The quantum critical point (QCP) $x_c \sim 0.63$ can be estimated from the interpolated $x$ value when $\rho_{yx}^0$ changes sign (fig. S6B). The solid symbols in Fig. 2G indicate the $T_C$ of each sample determined by the temperature when $H_{coer}$ becomes zero.

ARPES measurements on $Bi_{1.78}Cr_{0.22}(Se_xTe_{1-x})_3$ uncover a surprising feature. The ARPES band maps displayed in Fig. 3A were taken at $T = 120$ K, when all the samples are in the PM state. The Fermi level of all the samples lies above the Dirac point, which is consistent with the negative slope of the normal Hall effect. The three samples with $x \leq 0.52$ show well-defined gapless surface states with linear dispersions. The surface-state features can be better identified by the dual-peak structures around the Γ point in the momentum distribution curves (MDCs) (Fig. 3, G to I). As $x$ is increased to $x = 0.67$ (Fig. 3D), however, the surface state features can no longer be resolved, and a small energy gap starts to appear at the Γ point of the band structure. With further increase of $x$ up to $x = 1$, the surface states are always absent, whereas the gap amplitude keeps increasing. Because the surface states derive from the nontrivial bulk topology, their absence for $x \geq 0.67$ suggests that the bulk band structure in this regime is topologically trivial. Therefore, the ARPES results reveal a topological QPT, a transition from the TI to trivial band insulator, accompanying the magnetic QPT. The ARPES patterns are very similar to that in $BiTl(S_{1-\delta}Se_\delta)_2$ TIs, showing the topological QPT induced by S substitution of Se (*23*, *24*).

The topological QPT is also corroborated through density functional theory (DFT) calculations (*17*). The signature of a topological QPT in the bulk band structure, a gap closing point at the critical SOC strength, can be seen clearly in the DFT results on Cr-doped $Bi_2Se_3$ (fig. S7). The topological QPT is caused by the reduced SOC strength resulting from the Cr substitution

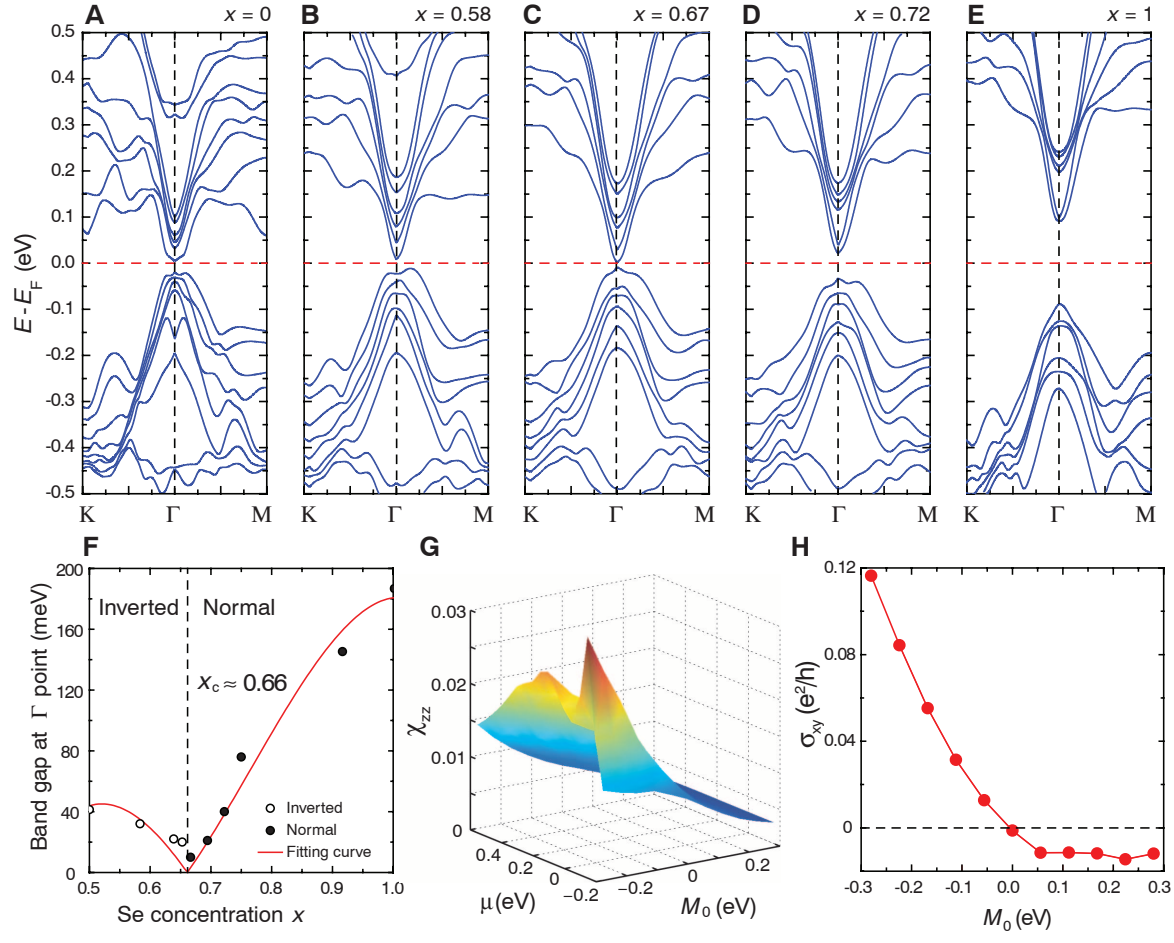


**Fig. 4.** Theoretical calculations of the band structure and magnetic properties. DFT-calculated bulk band structure of $Bi_{1.75}Cr_{0.25}(Se_xTe_{1-x})_3$, with (**A**) $x = 0$, (**B**) 0.58, (**C**) 0.67, (**D**) 0.72, and (**E**) 1.0. (**F**) The topological phase diagram. Between $x = 0.5$ and critical point $x_c = 0.66$, the bulk band structure is inverted. Above that, the band structure becomes normal. (**G**) The calculated spin susceptibility of the four-band model for different μ and $M_0$. (**H**) Anomalous Hall conductivity $\sigma_{xy}$ as a function of $M_0$ with $G_{z1} = 0$ and $G_{z2} = 0.02$ eV at fixed μ = 0.4 eV showing the sign reversal of $\sigma_{xy}$ across the topological QPT.

of Bi. At sufficiently high Cr doping, the SOC is not strong enough to invert the bands, leading to a trivial bulk topology (*19*). In contrast, for Cr-doped $Bi_2Te_3$ our DFT calculations show that the bulk band remains inverted for Cr content up to $y = 0.25$ (figs. S8 and S9). The more robust band inversion is a result of the larger SOC strength of Te as compared with Se. The calculated band structures of $Bi_{1.75}Cr_{0.25}(Se_xTe_{1-x})_3$ with varied $x$ (Fig. 4, A to E) show a transition from inverted to normal bands caused by the reduced SOC strength with increasing Se/Te ratio. The calculated bulk gap at the Γ point is summarized in Fig. 4F, which clearly shows a topological QPT near $x \sim 0.66$, which is in agreement with the experiments.

With the correlation between the magnetic and topological QPTs firmly established, we turned to a more fundamental question: Which phase transition is the driving force, and which one is the consequence? Two pieces of evidence support the scenario that topology determines the magnetic ordering. First, in our $Bi_{1.78}Cr_{0.22}(Se_xTe_{1-x})_3$ samples the Cr content is fixed, and only the Se/Te ratio is varied. This provides a knob for fine-tuning the SOC strength—hence, the bulk band topology—but the magnetic property is not directly affected. Therefore, the magnetic QPT should be a secondary effect of the topological QPT. Second, the ARPES results show that even at high $T$ when all the samples are in the PM state, the two regimes separated by the QCP already develop different topologies. At low $T$, the magnetic ground states form following the preformed topological character, with the FM phase resulting from the nontrivial topology and transitioning to the PM phase when the bulk turns topologically trivial.

The topological origin of the magnetic QPT is further supported by the effective model calculations (*17*). We calculated the $z$-direction spin susceptibility ($\chi_{zz}$) of eight QL magnetically doped TI films using an effective four-band model (Fig. 4G) as a function of the chemical potential (μ) and the mass term ($M_0$). In the inverted regime with $M_0 < 0$, $\chi_{zz}$ always remains a large value when μ is around the gap, as a consequence of the van Vleck mechanism (*5*); the second-order matrix element is strongly enhanced when the bulk bands become inverted. The topologically nontrivial phase thus strongly favors an FM ordering, which naturally explains the topology-driven magnetic QPT discovered in the experiments. The van Vleck mechanism is further supported by the magnetization measurements (fig. S10), which show that the ferromagnetism occurs in the bulk rather than on the surfaces (*25*, *26*). The out-of-plane magnetic anisotropy (fig. S11) is also consistent with the van Vleck–type FM order in TIs (*5*).

To reveal the physical origin of the AHE sign change at the QCP, we calculated $\sigma_{xy}$ based on the four-band model, with two additional Zeeman splitting terms, $G_{z1}$ and $G_{z2}$, from the exchange coupling between the electrons and magnetic impurities (*17*). The $\sigma_{xy}$ value is summarized in Fig. 4H as a function of $M_0$ with fixed chemical potential, which clearly uncovers a sign change when the band gap is reversed, which is in good agreement with the experimental observation. The close correlation between the sign of AHE and topological QPT suggests that it can be used as a transport fingerprint for the bulk topology. This is not unexpected given the growing recognition of the topological nature of the intrinsic AHE in recent years (*27*, *28*). The extrinsic AHE, which may be present in realistic materials, is ignored here because it typically dominates in highly metallic materials, whereas the disordered TI films studied here are poorly conductive (*20*).

The topologically nontrivial FM states with tunable magnetic properties revealed here provide an ideal platform for realizing the exotic magnetoelectric effects proposed by theory. The topology-driven magnetic QPT may also inspire new ideas for topological-magnetic phenomena and spintronic applications in TIs with broken TRS. We cannot completely rule out all other possibilities for the disappearance of FM ordering across the topological QPT. For example, the ARPES results (Fig. 3) show that the properties of itinerant carriers also change with Se content, which may affect an itinerant-driven FM mechanism.

### References and Notes


1. X. L. Qi, S. C. Zhang, *Phys. Today* **63**, 33 (2010).
2. M. Z. Hasan, C. L. Kane, *Rev. Mod. Phys.* **82**, 3045 (2010).
3. J. E. Moore, *Nature* **464**, 194 (2010).
4. X. L. Qi, R. Li, J. Zang, S. C. Zhang, *Science* **323**, 1184 (2009).
5. R. Yu *et al.*, *Science* **329**, 61 (2010).
6. K. Nomura, N. Nagaosa, *Phys. Rev. Lett.* **106**, 166802 (2011).
7. W. K. Tse, A. H. MacDonald, *Phys. Rev. Lett.* **105**, 057401 (2010).
8. I. Garate, M. Franz, *Phys. Rev. Lett.* **104**, 146802 (2010).
9. H. J. Zhang *et al.*, *Nat. Phys.* **5**, 438 (2009).
10. Y. Xia *et al.*, *Nat. Phys.* **5**, 398 (2009).
11. Y. L. Chen *et al.*, *Science* **325**, 178 (2009).
12. Y. S. Hor *et al.*, *Phys. Rev. B* **81**, 195203 (2010).
13. Y. L. Chen *et al.*, *Science* **329**, 659 (2010).
14. L. A. Wray *et al.*, *Nat. Phys.* **7**, 32 (2010).
15. Y. Okada *et al.*, *Phys. Rev. Lett.* **106**, 206805 (2011).
16. H. Beidenkopf *et al.*, *Nat. Phys.* **7**, 939 (2011).
17. Materials and methods are available as supplementary materials on *Science* Online.
18. Y. Zhang *et al.*, *Nat. Phys.* **6**, 712 (2010).
19. H. Jin, J. Im, A. J. Freeman, *Phys. Rev. B* **84**, 134408 (2011).
20. N. Nagaosa, J. Sinova, S. Onoda, A. H. MacDonald, N. P. Ong, *Rev. Mod. Phys.* **82**, 1539 (2010).
21. H. T. He *et al.*, *Phys. Rev. Lett.* **106**, 166805 (2011).
22. M. H. Liu *et al.*, *Phys. Rev. Lett.* **108**, 036805 (2012).
23. S. Y. Xu *et al.*, *Science* **332**, 560 (2011).
24. T. Sato *et al.*, *Nat. Phys.* **7**, 840 (2011).
25. Q. Liu, C. X. Liu, C. Xu, X. L. Qi, S. C. Zhang, *Phys. Rev. Lett.* **102**, 156603 (2009).
26. G. Rosenberg, M. Franz, *Phys. Rev. B* **85**, 195119 (2012).
27. J. Sinova, T. Jungwirth, J. Cerne, *Int. J. Mod. Phys. B* **18**, 1083 (2004).
28. A. MacDonald, Q. Niu, *Phys. World* **17**, 18 (2004).



**Acknowledgments:** We thank X. Dai, Z. Fang, and S. C. Zhang for helpful discussions. We thank Y. G. Zhao, P. S. Li, X. L. Dong, and Y. Wu for assistance with superconducting quantum interference device measurements. This work is supported by the Natural Science Foundation and Ministry of Science and Technology of China and the Chinese Academy of Sciences.


### Supplementary Materials

www.sciencemag.org/cgi/content/full/339/6127/1582/DC1
Materials and Methods
Supplementary Text
Figs. S1 to S17
References (*29*–*41*)


1 October 2012; accepted 22 January 2013
10.1126/science.1230905


# Ultrafast Tryptophan-to-Heme Electron Transfer in Myoglobins Revealed by UV 2D Spectroscopy


**Cristina Consani,[1]* Gerald Auböck,[1]* Frank van Mourik,[1] Majed Chergui[1]†**



**Tryptophan is commonly used to study protein structure and dynamics, such as protein folding, as a donor in fluorescence resonant energy transfer (FRET) studies. By using ultra-broadband ultrafast two-dimensional (2D) spectroscopy in the ultraviolet (UV) and transient absorption in the visible range, we have disentangled the excited state decay pathways of the tryptophan amino acid residues in ferric myoglobins (MbCN and metMb). Whereas the more distant tryptophan ($Trp^7$) relaxes by energy transfer to the heme, $Trp^{14}$ excitation predominantly decays by electron transfer to the heme. The excited $Trp^{14}$→heme electron transfer occurs in <40 picoseconds with a quantum yield of more than 60%, over an edge-to-edge distance below ~10 angstroms, outcompeting the FRET process. Our results raise the question of whether such electron transfer pathways occur in a larger class of proteins.**


The advent of optical-domain multidimensional spectroscopies has opened entirely new perspectives for the study of biochemical dynamics, thanks to their abilities to visualize correlations and interactions between chromophores of the protein (*1*). This is particularly interesting when it comes to finding the pathways of electron and/or energy transfer in proteins, which are key processes in bioenergetics. Whereas vibrational multidimensional spectroscopy in the infrared (IR), which detects the couplings between vibrational dipoles, was established in the early 1990s, it was only in mid-2000 that the first study


[1]Laboratory of Ultrafast Spectroscopy, École Polytechnique Fédérale de Lausanne, CH-1015 Lausanne, Switzerland.

*These authors contributed equally to this work.
†Corresponding author. E-mail: majed.chergui@epfl.ch